

Copyright
by
John William Peterson
2003

**A Numerical Investigation of Bénard Convection in
Small Aspect Ratio Containers**

by

John William Peterson, B.S.

REPORT

Presented to the Faculty of the Graduate School of
The University of Texas at Austin
in Partial Fulfillment
of the Requirements
for the Degree of

MASTER OF SCIENCE IN ENGINEERING

THE UNIVERSITY OF TEXAS AT AUSTIN

May 2003

**A Numerical Investigation of Bénard Convection in
Small Aspect Ratio Containers**

APPROVED BY

SUPERVISING COMMITTEE:

Graham F. Carey, Supervisor

Anand L. Pardhanani

For Loriele.

Acknowledgments

I wish to thank all of my colleagues in the CFDLAB, most notably Benjamin Kirk and Bill Barth, for many useful discussions at the white board and moral support. This work has been supported by grant number NGT5-139, as part of the NASA Graduate Student Fellowship Program.

A Numerical Investigation of Bénard Convection in Small Aspect Ratio Containers

John William Peterson, MSE
The University of Texas at Austin, 2003

Supervisor: Graham F. Carey

Numerical simulations of combined buoyant and surface-tension-driven (Rayleigh-Bénard-Marangoni) flow are conducted for heated fluid layers of small aspect ratio (defined as the horizontal extent of the domain divided by the depth of the fluid) in polygonal containers. Classical results from linear stability analysis are discussed in the context of small aspect ratio containers, and used to define a significant region of the parameter space spanned by the Marangoni number Ma (a surface tension parameter), the Rayleigh number Ra (a buoyancy parameter) and the aspect ratio Γ . The Galerkin finite element formulation for the coupled incompressible Navier-Stokes and heat transfer equations is given, and implementation aspects are briefly discussed. Numerical results displaying distinct steady-state patterns containing between 1 and 8 convection cells are given for a range of aspect ratios between 3 and 11. The appearance of pentagonal and hexagonal convective cells are discussed, and some of the properties of the transition to the fully hexagonal convection regime are noted.

Table of Contents

Acknowledgments	v
Abstract	vi
List of Tables	ix
List of Figures	x
Chapter 1. Introduction	1
1.1 Historical Perspective	1
1.2 Practical Applications	3
1.3 Objectives and Outline	4
Chapter 2. Linear Theory	6
2.1 Pure Surface-Tension-Driven Convection	6
2.1.1 Physical Considerations	6
2.1.2 Linear Stability Analysis	7
2.1.3 Discussion	11
2.2 Combined Buoyant and Surface-Tension-Driven Convection . .	11
2.2.1 Physical considerations	12
2.2.2 Linear Stability Analysis	12
2.2.3 Discussion	13
Chapter 3. Non-dimensionalization of the Governing Equations	16
3.1 Motivation	16
3.2 Generic non-dimensionalization of the weak form	17
3.2.1 Momentum Equation	17
3.2.2 Continuity Equation	20
3.2.3 Energy Equation	21

3.3	The Classical Approach	21
3.4	A Different Approach – Surface Tension Velocity	23
Chapter 4.	Numerical Method	26
4.1	Non-dimensionalization	28
4.2	Finite Element Method	30
4.3	Solution Method	32
4.4	Computational Aspects	33
Chapter 5.	Results	34
5.1	Cellular Patterns With Increasing Aspect Ratio	34
5.2	Intermediate Steady States	38
	Bibliography	44
	Vita	48

List of Tables

4.1	Boundary conditions on the governing equations	26
4.2	Non-dimensionalized boundary conditions	29

List of Figures

1.1	Henri Bénard’s original test apparatus.	1
1.2	One of the first pictures of Bénard convection cells	2
2.1	Linear stability diagram, after Nield (1964)	15
5.1	1,2,3,4-cell patterns $Ma = 92$, $Ra = 30$	36
5.2	5,6,7,8-cell patterns for $Ma = 92$, $Ra = 30$	37
5.3	4-cell “clover” pattern	38
5.4	6-cell pattern displaying pentagonal cell	39
5.5	7-cell pattern displaying hexagonal cell	41
5.6	10-cell pattern	42

Chapter 1

Introduction

1.1 Historical Perspective

Bénard convection, sometimes referred to as Bénard-Marangoni convection (and inaccurately referred to as Rayleigh-Bénard convection) was first observed by Henri Bénard [2] near the turn of the 20th century. His experimental apparatus was designed to study the behavior of thin layer of spermaceti (whale oil) on a metallic plate suspended above a boiling water bath at approximately 100°C. A schematic drawing of Bénard's test apparatus is given in Figure 1.1.

In this experiment, the horizontal extent of the spermaceti surface was much greater than its depth, and Bénard observed the ordered formation of hexagonal cells far away from the boundaries of the container. He determined correctly that warm fluid was flowing up in the centers of the convection cells, and down the

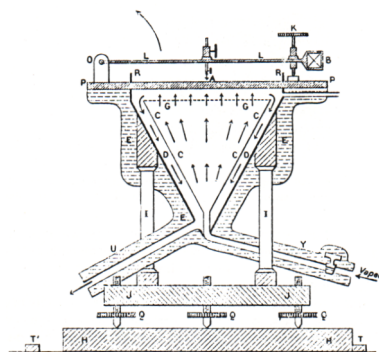


Figure 1.1: Henri Bénard's original test apparatus. A metallic plate of length L covered with a layer of spermaceti of depth $d \ll L$ is suspended over a container of approximately 100°C water vapor. Reproduced in [16].

hexagonal boundaries. Furthermore, the height of the surface itself varied on the order of 1 micron over the cells themselves. Bénard attributed the striking patterns shown in Figure 1.2 (incorrectly) to flow due to buoyant forces acting in the bulk of the fluid. Rayleigh [23] later confirmed, through linear stability analysis, that buoyant forces do in fact generate convective cells. His findings, however, do not strictly apply to the configurations investigated by Bénard.

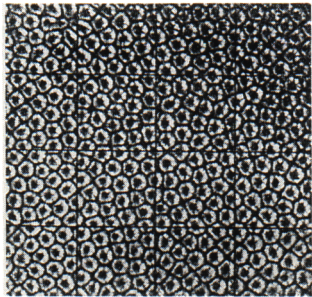


Figure 1.2: One of the first pictures of Bénard convection cells, taken by Bénard himself during the experiments described in [2].

Bénard's incorrect conclusion was not categorically dismissed for at least another fifty years, at which time it was shown experimentally by Block [3] in 1956, and theoretically by Pearson [22] in 1958 that changes in surface tension, due to minor variations in the temperature of the fluid surface, were actually causing the convective cells noted in these two thin layer problems. Since that time, the linear stability of such configurations has been well-analyzed, especially in the case of a layer of infinite horizontal extent i.e. aspect ratio ap-

proaching infinity. These works have led to a deeper understanding of the fundamental physics at work in the problem, and to categorizations of so-called critical and threshold parameters important to convection.

Until recently, linear stability analysis of small aspect-ratio containers has not been possible because of the need to solve numerically a relatively

large linear system of equations as in the work of Dijkstra [8]. New theoretical results, numerical simulations, and experimental work are still needed to gain a more fundamental understanding of the problem.

1.2 Practical Applications

The practical applications of surface-tension-driven flow are many and varied, and help to explain the sustained interest in the topic since Bénard’s work at the turn of the century. In the realm of chemical engineering applications, Dijkstra [7] mentions two applications [21, 25] in which mass transfer across an interface is strongly influenced by surface tension effects.

Another application where surface tension is important is silicon crystal growth by the float-zone technique [24]. In this process, solid silicon crystals are “grown” from a molten silicon solution suspended between two moving furnace coils [5]. An advantage of this technique is that the purity of the resulting crystal is improved because the silicon does not come into contact with exterior containers. A drawback is surface tension forces alone are required to support the total weight of the silicon solution contained in the melt zone. Optimization of the surface tension field through the use of heating devices as well as the utilization the float-zone crystal growth technique in microgravity environments, may be able to produce higher quality, more economical silicon wafers in the semiconductor industry.

These applications are certainly not all of the industrial processes which rely on surface tension as an important physical aspect. Others, including the

quality of metallic welds, the creation of compact disc media by heating the surface of the disc with a laser, and microfluidics/nanomechanics applications are under active investigation as well. Clearly combined buoyant and surface-tension driven flows are of considerable engineering importance.

1.3 Objectives and Outline

A standard method for describing the behavior of the convective cells (their number, shape, and strength) as functions of the Rayleigh number (“ Ra ”, a non-dimensional parameter governing buoyant forces), the Marangoni number (“ Ma ”, a non-dimensional parameter governing surface tension forces) and the aspect ratio (so-called “ Γ ”) of small aspect ratio containers apparently does not currently exist.

The main objective of this report is to gain a better understanding of the physics driving the different convective patterns which arise in small aspect ratio containers. This includes both the reproduction of classical experimental results for a range of different container sizes, as well as a classification of the initial formation of cells with distinctive geometric configurations, most importantly the development of pentagonal and hexagonal cells as well as the combination of these shapes during transition from small to intermediate aspect ratio containers.

The remaining sections of this report are arranged in the following manner: Chapter 2 details the classical linear stability theory results for the pure surface-tension-driven case and the combined buoyant surface-tension-driven

cases. Chapter 3 discusses the important topic of non-dimensionalization of the governing equations, and some of the scaling conclusions which can be drawn from simple manipulation of the particular length and time scales. Chapter 4 covers the numerical methods used in the investigation, including the finite element formulation and some computational aspects. Finally, Chapter 5 presents the results of several numerical simulations as well as a discussion of their role in furthering the understanding of surface-tension-driven convection.

Chapter 2

Linear Theory

2.1 Pure Surface-Tension-Driven Convection

The following sections summarize the basic fluid properties and results from linear stability analysis for pure surface-tension-driven convection in domains of infinite horizontal extent. The original derivation was completed by Pearson [22] in 1958, and is summarized in many reference works on Bénard cells, including that of Koschmieder [16].

2.1.1 Physical Considerations

We consider a fluid (typically a liquid) with a free surface in contact with another fluid (typically a gas) e.g. a silicon oil (high Pr) liquid bed in contact with air. The most important property of the fluid-gas interface under consideration is the quantification of the surface tension at the interface, measured in units of force per unit distance, and symbolized by γ .

The surface tension varies with the temperature T of the interface, and is well-represented with the truncated Taylor series given by:

$$\gamma(T) = \gamma_0 + \frac{\partial \gamma}{\partial T} T \quad (2.1)$$

since for most fluids this variation is nearly linear. The parameter most important in determining the onset of convection is the rate $\frac{\partial\gamma}{\partial T} < 0$ in Eqn (2.1).

Therefore, any disturbance of the temperature on the surface of the liquid will generate a shear stress on the free surface. If, as is usually the case, the slope $\frac{\partial\gamma}{\partial T}$ in Eqn (2.1) is negative, then the surface tension of the liquid decreases with temperature, and fluid will be moved by surface shear stress from warm regions toward cooler regions (the Marangoni effect).

In experiments, especially for large aspect-ratio systems, a variation in the height of the free surface itself also accompanies the warm and cold spots on the surface. This fact was noted in the early work of Bénard [2] as well. The surface motions in these experiments are small and in the present mathematical model are presumed negligible. This assumption is also consistent with other modeling and simulation work on this problem class [18, 22, 23].

Thermal energy supplied to the system is converted to kinetic energy and fluid motion due to thermocapillary surface tension and buoyancy. Heat is also conducted through the layer and away at the top surface. To reduce experimental uncertainty in cooling patterns at the top surface, a thin air layer is typically maintained just below an active cooling device, such as a water-cooled sapphire window [9].

2.1.2 Linear Stability Analysis

Linear stability theory is applied to the Navier-Stokes, continuity, and energy equations for a fluid of infinite horizontal extent and uniform thickness,

with a free, non-deformable upper surface (subject to surface tension effects) and a stationary (no-slip) lower surface. It is further assumed that the effects of buoyancy are negligible ($Ra \approx 0$) typically because of the fact that extremely thin fluid layers are used.

The initial configuration is that of a fluid layer at rest with a linear vertical conducting temperature profile whose constant gradient is given by $\Delta T/d$, where ΔT is the difference between the top and bottom temperatures, and d is the height of the fluid layer. The fluid layer is disturbed with infinitesimal velocity and temperature perturbations, small enough that the convective terms in the Navier-Stokes equation may be neglected. The classic perturbation equations originally given in the work of Pearson [22] are:

$$\left(\frac{\partial}{\partial t} - \nu \nabla^2\right) \nabla^2 w = 0 \quad (2.2)$$

$$\left(\frac{\partial}{\partial t} - \alpha \nabla^2\right) \theta = \frac{\Delta T}{d} w \quad (2.3)$$

where w is the vertical component of the velocity, $\nu = \mu/\rho$ is the kinematic viscosity, α is the thermal diffusivity of the fluid, and θ is the variation from the linear temperature profile. This linear fourth-order system of equations has the following boundary conditions on velocity:

$$\begin{aligned} z = 0 : \quad & w = 0, \quad \frac{\partial w}{\partial z} = 0 \\ z = 1 : \quad & w = 0, \quad \rho \nu \frac{\partial^2 w}{\partial^2 z} = -\frac{\partial \gamma}{\partial T} \nabla^2 \theta \end{aligned}$$

and for the thermal equation:

$$\begin{aligned} z = 0 : \quad & \theta = 0 \\ z = 1 : \quad & \frac{\partial \theta}{\partial z} = -\frac{q}{k}\theta \end{aligned}$$

where k is the thermal conductivity of the fluid, and q represents the heat flux from the upper surface of the fluid due to the small temperature disturbances (not the imposed linear profile). For an insulating air layer, q may be set to zero. We proceed by trying product solutions of the form:

$$w(x, y, z, t) = -\frac{\alpha}{d}W(z)f(x, y)e^{st} \quad (2.4)$$

$$\theta(x, y, z, t) = \Delta T \Theta(z)f(x, y)e^{st} \quad (2.5)$$

for a particular growth rate s . We note that since surface tension gradients are not present in these forms of the disturbances, the pattern which ultimately forms from these disturbances must be due to fluctuations in the fluid layer itself, not on the surface. These product solutions are identical to those used in the earlier work done by Rayleigh [23] on buoyancy-driven flow.

Assuming that the disturbance pattern is periodic in x and y , the function $f(x, y)$ above satisfies the so-called membrane equation, given by:

$$\nabla^2 f(x, y) + a^2 f(x, y) = 0 \quad (2.6)$$

where a is the wave number for the disturbance. After non-dimensionalization with characteristic length scale d and characteristic time scale d^2/α , and sub-

stituting in Eqn (2.6), the linear equations for neutral stability ($s = 0$) become:

$$\left(\frac{d^4}{dz^4} - a^4\right)W = 0 \quad (2.7)$$

$$\left(\frac{d^2}{dz^2} - a^2\right)\Theta = -W \quad (2.8)$$

with non-dimensionalized boundary conditions for the momentum equation:

$$z = 0 : \quad W = 0, \quad \frac{dW}{dz} = 0 \quad (2.9)$$

$$z = 1 : \quad W = 0, \quad \frac{d^2W}{dz^2} = a^2 Ma \Theta \quad (2.10)$$

and the thermal equation:

$$z = 0 : \quad \Theta = 0 \quad (2.11)$$

$$z = 1 : \quad \frac{d\Theta}{dz} = -Bi\Theta \quad (2.12)$$

where $Ma = \frac{\partial\gamma}{\partial T} \frac{\Delta T d}{\rho\nu\alpha}$ is the Marangoni number and $Bi = \frac{qd}{k}$ is the Biot number, a non-dimensional heat flux. After substituting for W in Eqn (2.7), it is possible to solve the resulting 6th-order linear ordinary differential equation for Θ , and subsequently back out W from Eqn (2.8). Details for various methods of solution can be found in [19, 22, 23]. The boundary conditions given in Eqns (2.9)–(2.12) lead to an analytic solution consisting of the hyperbolic trigonometric functions.

For given values of Ma and Bi , critical values of the wave number, a_{crit} can be determined. Marginal stability (conduction/convection) curves based on values of a_{crit} for different values of Ma can then be constructed and analyzed. In general, the larger Bi , the larger ΔT is required before the onset of convection. For $Bi = 0$, the critical Ma is $Ma_c \approx 79.607$.

2.1.3 Discussion

While Ma_c is useful in developing a baseline simulation in which convection due to surface tension will at least be present, the above result applies to layers of infinite horizontal extent. The no-slip boundary conditions present on the lateral walls of small aspect ratio containers have been shown [17] to significantly impact the formation of cellular patterns.

Furthermore, in the work of Dijkstra [8] it has been demonstrated through numerical linear stability analysis of the perturbation equations in small aspect ratio containers that the critical Marangoni number increases as the aspect ratio of the box decreases, with, e.g., a value of $Ma_c \approx 130$ for an aspect ratio of 1.5. Although we will be solving the full nonlinear equations in the present work, these linear analyses provide an excellent starting point for determining valid parameter ranges.

2.2 Combined Buoyant and Surface-Tension-Driven Convection

We now discuss some of the theoretical results for the case of combined buoyant and surface-tension-driven convection, first given in the work of Nield [19]. This topic warrants some explanation, since in earth-based laboratory experiments gravitational effects are present even for very thin fluid layers (although this importance diminishes as the layer thickness decreases). The results of the analysis are also quite interesting because they suggest that buoyancy and surface tension effects do not act independently, but are in re-

ality quite tightly coupled.

2.2.1 Physical considerations

We consider again a fluid layer of infinite horizontal extent with a free surface which is subject to the temperature-varying surface-tension condition described by Eqn (2.1). The fluid is also subject to buoyant forces in the bulk because of the vertical temperature variation. In physical terms, this means that warmer fluid tends to rise while cooler fluid tends to sink. This buoyant force may be modeled using the Boussinesq approximation, associated with the thermal expansion of the fluid. The formal definition of the thermal expansion coefficient β is related to the first term in the Taylor series expansion of ρ as a function of temperature, and follows as:

$$\beta = -\frac{1}{\rho} \frac{\partial \rho}{\partial T} \quad (2.13)$$

and can be assumed constant for this work.

The Boussinesq approximation introduces an additional term in the linearized momentum equation (2.2) which results in a new coupling between temperature and velocity that will be explored in the next section.

2.2.2 Linear Stability Analysis

Beginning with the same initial configuration for the fluid layer as in the last case, and considering infinitesimal disturbances to the system, we again

arrive at the set of coupled linearized momentum and energy equations:

$$\left(\frac{\partial}{\partial t} - \nu \nabla^2\right) \nabla^2 w = g_z \beta \nabla^2 \theta \quad (2.14)$$

$$\left(\frac{\partial}{\partial t} - \alpha \nabla^2\right) \theta = \frac{\Delta T}{d} w \quad (2.15)$$

where g_z is the z -component of the local gravity vector. We note that these equations are identical to Eqns (2.2) and (2.3) except for the term on the right-hand side of Eqn (2.14) which is the buoyant coupling term alluded to previously. The boundary conditions in this case are identical to those of the previous case, as are the assumed forms of the product solutions given by Eqns (2.4) and (2.5). After non-dimensionalization in a similar manner to that applied previously, the analog of Eqns (2.7) and (2.8) are:

$$\left(\frac{d^4}{dz^4} - a^4\right) W = a^2 Ra \Theta \quad (2.16)$$

$$\left(\frac{d^2}{dz^2} - a^2\right) \Theta = -W \quad (2.17)$$

where $Ra = g_z \beta \Delta T d^3 / \alpha \nu$ is the Rayleigh number. When combined with the non-dimensionalized boundary conditions given in Eqns (2.9) through (2.12) the linearized formulation of the combined buoyant and surface-tension driven convection problem is completed.

2.2.3 Discussion

Solution of Eqns (2.16) and (2.17) is not as straight-forward as that of the pure surface-tension driven equations (2.7) and (2.8), but is possible, as shown by Nield [19], by employing clever manipulations of Fourier series.

The stability results derived from this solution are quite interesting, and show a strong coupling between Ra and Ma . The conditional stability solution is given in Figure 1 of Nield’s paper, and for the insulating upper boundary case ($Ma_c = 79.607, Ra_c = 669$) we find the rather surprising result that the locus of points approximately satisfies:

$$\frac{Ra}{Ra_c} + \frac{Ma}{Ma_c} \approx 1 \quad (2.18)$$

i.e. the stable (conducting) and unstable (convection) regimes of the solution are separated in the Ra – Ma parameter space according to the neutral stability line shown in Figure 2.1.

This linear stability result is an important consideration for the numerical studies conducted for this report. It shows that convection may occur at subcritical values of *both* the Rayleigh and Marangoni numbers when buoyancy and surface tension are present. This direct reinforcement by the two sources of motion is difficult to explain with physical arguments, but it shows that a tight coupling between the fluid surface and the bulk is present. It also implies that reproduction of earth-based experiments in the presence of gravity will be difficult without consideration of the buoyancy terms as well.

We note finally in closing that these results are only strictly valid for fluid layers of infinite extent, and that the coupling between the surface tension and buoyant forces need not extend in general to containers of finite extent or small aspect ratio, although we do expect some correlation. As in the previous section for pure surface tension driven flow, we again stress the importance

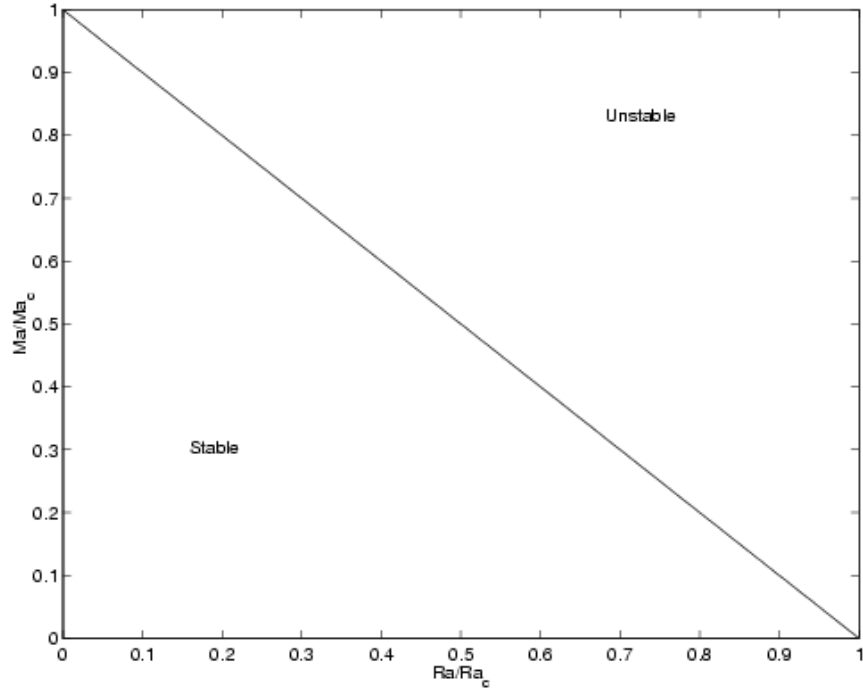


Figure 2.1: The approximate stability result of Nield [19], showing the tight coupling between buoyant and surface tension driven phenomena. Davis [6] later confirmed Nield’s linear Fourier analysis using the “Method of Energy,” and also showed a possible region of sub-critical instabilities below the linear curve.

of these linear analyses insofar as they generate a qualitative understanding of certain aspects of the solution to problem, but we need accurate numerical simulations to gather important details and nuances about the flow.

Chapter 3

Non-dimensionalization of the Governing Equations

3.1 Motivation

Since the early work of Bénard, it has since been shown [19, 22] that in thin fluid layers with a free surface, surface tension effects (more so than buoyant effects) are the dominant parameter governing convective instabilities. In such situations, the amount of space into which the convective cells must “fit” seems to define a more fundamental length scale than the depth of the fluid domain. The motivation, therefore, of attempting to find an alternate set of non-dimensional parameters than were originally used by Rayleigh is to perhaps gain additional insight into the fundamental physical aspects of the problem.

In order to avoid the definition of (yet another!) non-dimensional parameter, and recognizing that an infinite set of possible non-dimensional parameters do exist for the coupled Navier-Stokes/heat transfer equations (see, for example [4]) we believe that any new set of parameters must simply be cast in terms of the traditional set made up of Ra , Ma , Γ , and Pr . Therefore we attempt to restrict ourselves in the following discussion only to re-groupings

of the classical parameters.

3.2 Generic non-dimensionalization of the weak form

In this section, we will consider a non-dimensionalization of the weak form of the coupled incompressible Navier-Stokes and heat-transfer equations. Without stating explicit physical parameters for scaling the problem, we will assume that we have been provided with appropriate length (l_s), time (t_s), velocity (u_s), and temperature (T_s) scales. After the derivation of the equations, we may choose specific values for these scaling parameters to determine the final form of the equations.

3.2.1 Momentum Equation

The momentum equations are a nonlinear set of vector-valued equations in the unknowns $\{\mathbf{u}, p, T\}$. Here $\mathbf{u}(\mathbf{x}, t)$ is the velocity vector, $p(\mathbf{x}, t)$ is the pressure, and T is temperature. In the following derivation we will consider the x -component of these equations; extension to the other directions follows directly. The x -momentum equation written in “divergence” or “conservative” form is given by:

$$\rho \frac{Du}{Dt} = \nabla \cdot \boldsymbol{\sigma}_x + \rho \beta g (T - T_{ref}) \quad (3.1)$$

where $\boldsymbol{\sigma}_x$ is the x -component row of the stress tensor, defined as:

$$\boldsymbol{\sigma}_x = \begin{bmatrix} 2\mu \frac{\partial u}{\partial x} - p & \mu \frac{\partial u}{\partial y} + \mu \frac{\partial v}{\partial x} & \mu \frac{\partial u}{\partial z} + \mu \frac{\partial w}{\partial x} \end{bmatrix} \quad (3.2)$$

for Newtonian fluids. Equations (3.1) and (3.2) use the standard symbols; ρ is the fluid density, $D/Dt = \partial/\partial t + (\mathbf{u} \cdot \nabla)$ is the total or material derivative, u is the x -component of the velocity vector, t is time, μ is the molecular viscosity, p is the pressure, β is the coefficient of thermal expansion for the fluid, T_{ref} is a reference buoyant temperature for the fluid, and g_x is the x -component of the gravity vector. Note: $g_x = g_y = 0$ in the simulations discussed in this report, hence the Boussinesq term will be zero in the x and y -momentum equations. The following derivation will retain the term for clarity of description.

We now proceed to derive the weak form by multiplying by a suitable test function, ϕ , and integrating over the domain of interest, Ω , to obtain:

$$\begin{aligned}
\int_{\Omega} \phi \left\{ \rho \frac{Du}{Dt} - \rho \beta g_x (T - T_{ref}) \right\} dV &= \int_{\Omega} \phi (\nabla \cdot \boldsymbol{\sigma}_x) dV \\
&= \int_{\Omega} \nabla \cdot (\phi \boldsymbol{\sigma}_x) dV - \int_{\Omega} \nabla \phi \cdot \boldsymbol{\sigma}_x dV \\
&= \int_{\partial\Omega} \phi \mathbf{n} \cdot \boldsymbol{\sigma}_x dS - \int_{\Omega} \nabla \phi \cdot \boldsymbol{\sigma}_x dV
\end{aligned} \tag{3.3}$$

where we have used the divergence theorem to get the last line. This is a convenient form of the equations to apply the traction boundary conditions on the flat free surface, specifically:

$$\mathbf{n} \cdot \boldsymbol{\sigma}_x = \frac{\partial \gamma}{\partial T} \frac{\partial T}{\partial x} \tag{3.4}$$

where $\frac{\partial \gamma}{\partial T}$ is the (assumed constant) change in the fluid's surface tension with temperature. The test function ϕ must be restricted to vanish on the parts of

$\partial\Omega$ for which Dirichlet data are specified. This implies that only the surface integral over the free surface remains as a boundary term. Rearranging this result gives:

$$\int_{\Omega} \left\{ \phi \left(\rho \frac{Du}{Dt} - \rho \beta g_x (T - T_{ref}) \right) + (\nabla \phi \cdot \sigma_x) \right\} dV = \int_{surf.} \phi \frac{\partial \gamma}{\partial T} \frac{\partial T}{\partial x} dS \quad (3.5)$$

In order to non-dimensionalize this weak form, we may define the following dimensionless “starred” variables, based on the generic scaling parameters:

$$\begin{aligned} \nabla^* &= \frac{1}{l_s} \nabla & T^* &= \frac{T}{T_s} & t^* &= \frac{t}{t_s} \\ u^* &= \frac{u}{u_s} = \frac{u}{l_s/t_s} \end{aligned}$$

With these substitutions, and the proper free surface boundary condition of Eqn (3.4), Eqn (3.5) becomes:

$$\begin{aligned} \int_{\Omega^*} \left\{ \phi \left(\rho \frac{u_s}{t_s} \frac{Du^*}{Dt^*} - \rho \beta g_x T_s (T^* - \frac{T_{ref}}{T_s}) \right) + \frac{\mu}{l_s t_s} (\nabla^* \phi \cdot \sigma_x^*) \right\} l_s^3 dV^* = \\ \int_{surf.}^* \phi \frac{\partial \gamma}{\partial T} \frac{T_s}{l_s} \frac{\partial T^*}{\partial x^*} l_s^2 dS^* \end{aligned} \quad (3.6)$$

where we have also made the substitutions:

$$\begin{aligned} \sigma_x^* &= \frac{\mu}{t_s} \left[2 \frac{\partial u^*}{\partial x^*} - p^* \quad \frac{\partial u^*}{\partial y^*} + \frac{\partial v^*}{\partial x^*} \quad \frac{\partial u^*}{\partial z^*} + \frac{\partial w^*}{\partial x^*} \right] \\ dV &= l_s^3 dV^* \\ dS &= l_s^2 dS^* \end{aligned} \quad (3.7)$$

and further assumed the test function and normal vector to be effectively dimensionless. To minimize the number of resulting non-dimensional groups,

we choose to make the coefficient in front of the stress term vanish. This is accomplished by multiplying Eqn (3.6) by $\frac{t_s}{\mu l_s^2}$ to obtain:

$$\int_{\Omega^*} \left\{ \phi \left(\rho \frac{u_s l_s}{\mu} \frac{Du^*}{Dt^*} - \frac{\rho \beta g_x T_s l_s t_s}{\mu} \left(T^* - \frac{T_{ref}}{T_s} \right) \right) + (\nabla^* \phi \cdot \boldsymbol{\sigma}_x^*) \right\} dV^* = \int_{surf.}^* \phi \frac{\partial \gamma}{\partial T} \frac{t_s T_s}{\mu l_s} \frac{\partial T^*}{\partial x^*} dS^* \quad (3.8)$$

By examining Eqn (3.8) we find that we are left with the following three non-dimensional groups, for which we need to choose labels:

$$\begin{aligned} \text{Group A} &= \frac{\rho u_s l_s}{\mu} \\ \text{Group B} &= \frac{\rho \beta g_x T_s l_s t_s}{\mu} \\ \text{Group C} &= \frac{\partial \gamma}{\partial T} \frac{t_s T_s}{\mu l_s} \end{aligned}$$

3.2.2 Continuity Equation

The strong form of the mass conservation (or continuity) equation for an incompressible fluid is given by:

$$\nabla \cdot \mathbf{u} = 0 \quad (3.9)$$

Introducing appropriate non-dimensional variables as in the previous section, multiplying by a suitable test function ψ , and integrating over Ω yields:

$$\int_{\Omega^*} \psi (\nabla^* \cdot \mathbf{u}^*) dV^* = 0 \quad (3.10)$$

The continuity equation does not introduce non-dimensional parameters as they may always be scaled through on the right hand side.

3.2.3 Energy Equation

The energy equation closes the Navier-Stokes system by providing a fifth equation which couples \mathbf{u} and T . The strong form is given by:

$$\rho c_p \frac{DT}{Dt} - \nabla \cdot (k \nabla T) = 0 \quad (3.11)$$

where c_p is the specific heat of the fluid and k is its thermal conductivity. Again multiplying by a suitable test function ϕ , integrating over Ω , and employing the divergence theorem gives:

$$\int_{\Omega} \left\{ \phi \rho c_p \frac{DT}{Dt} + (\nabla \phi \cdot k \nabla T) \right\} dV = \int_{free\ surf.} k \phi (\nabla T \cdot \mathbf{n}) dS \quad (3.12)$$

Introducing the non-dimensional “starred” variables as before, Eqn (3.12) becomes:

$$\int_{\Omega^*} \left\{ \phi \left(\frac{\rho c_p l_s^2}{t_s k} \right) \frac{DT^*}{Dt^*} + (\nabla^* \phi \cdot \nabla^* T^*) \right\} dV^* = \int_{free\ surf.}^* \phi (\nabla^* T^* \cdot \mathbf{n}) dS^* \quad (3.13)$$

We have now introduced one additional generic non-dimensional group

$$\text{Group D} = \frac{\rho c_p l_s^2}{t_s k} = \frac{l_s^2}{\alpha t_s} \quad (3.14)$$

where the thermal diffusivity $\alpha = k/\rho c_p$ has been substituted.

3.3 The Classical Approach

The classical treatment of the problem proceeds as follows: prescribe the length scale of the problem, l_s , to be the physical depth d of the problem domain. In order to generate a time scale for the problem, the thermal diffusivity of the liquid, called α here, is employed. Specifically t_s is defined as

d^2/α to imply that the fluid motion occurs on the time scale of heat diffusion rather than momentum diffusion (typically defined by the kinematic viscosity ν .) The relevant velocity scale u_s is implied by these length and time scales. Finally, the temperature scale T_s is typically defined as ΔT , the temperature difference which is imposed on the problem domain.

With these scaling choices we arrive at the following (classical) set of non-dimensional parameters:

$$\begin{aligned}
\text{Group A} &= \frac{\rho u_s l_s}{\mu} = \frac{\alpha \rho}{\mu} = \frac{\alpha}{\nu} = \frac{1}{Pr} \\
\text{Group B} &= \frac{\rho \beta g_x T_s l_s t_s}{\mu} = \frac{\rho \beta g_x \Delta T d^3}{\alpha \mu} = \frac{\rho^2 c_p \beta g_x \Delta T d^3}{k \mu} = Ra \\
\text{Group C} &= \frac{\partial \gamma}{\partial T} \frac{t_s T_s}{\mu l_s} = \frac{\partial \gamma}{\partial T} \frac{d \Delta T}{\mu \alpha} = \frac{\partial \gamma}{\partial T} \frac{\rho c_p d \Delta T}{k \mu} = Ma \\
\text{Group D} &= \frac{l_s^2}{\alpha t_s} = \frac{d^2}{\alpha (d^2/\alpha)} = 1
\end{aligned}$$

Groups A, B, and C have also been labeled with their traditional names, the inverse of the Prandtl number, the Rayleigh number, and the Marangoni number. These parameters are quite useful in practice and experimentalists typically report values of Ra and Ma for each geometry which they investigate. Pr depends only on the fluid properties, and is typically constant for a given set of experiments.

We may also, for comparison purposes, reduce or even “turn off” the effects of surface tension in this formulation by setting $Ma = 0$. Therefore the set of equations defined by Eqn (3.8) in addition to the suitably non-dimensionalized continuity and energy equations, form a flexible system which

may be used for computational investigations of buoyancy-driven Rayleigh-Bénard (RB), surface-tension-driven Bénard-Marangoni (BM), and combined buoyant and surface-tension-driven Rayleigh-Bénard-Marangoni (RBM) flows. At the cost of some of this generality, we shall show in the next section that a different set of equations may also be derived.

3.4 A Different Approach – Surface Tension Velocity

Here we attempt to create another equivalent set of equations which may be particularly useful when surface tension effects are quite dominant, i.e. when Ma is approximately equal to, or perhaps much greater than, Ra . We will only expect to be able to use these equations for RBM or BM flow, and expect them to work best when Ra is small.

We begin by examining Group C above, and scaling so that:

$$\text{Group C} = \frac{\partial\gamma}{\partial T} \frac{t_s T_s}{\mu l_s} = \frac{\partial\gamma}{\partial T} \frac{T_s}{\mu} \frac{1}{u_s} = 1 \quad (3.15)$$

in other words,

$$u_s = \frac{\partial\gamma}{\partial T} \frac{T_s}{\mu} \quad (3.16)$$

becomes our relevant velocity scale. We refer to this as our “surface tension velocity,” and note in particular that it has no dependence on the depth of the domain. By again introducing the thermal diffusivity α , we find that:

$$l_s = \frac{\alpha}{u_s} = \frac{k\mu}{\rho c_p \frac{\partial\gamma}{\partial T} T_s} \quad (3.17)$$

is our relevant length scale. The reason for this choice of l_s is two-fold: it follows the precedent set by the classical formulation, and it avoids introducing

an additional non-dimensional parameter in the energy equation. The time scale t_s is implied by these choices for u_s and l_s . By again choosing ΔT for the relevant temperature scale, we now obtain the following non-dimensional parameters:

$$\begin{aligned}
\text{Group A} &= \frac{\rho u_s l_s}{\mu} = \frac{\rho}{\mu} \frac{\frac{\partial \gamma}{\partial T} \Delta T}{\mu} \frac{k \mu}{\rho c_p \frac{\partial \gamma}{\partial T} \Delta T} = \frac{k}{\mu c_p} = \frac{1}{Pr} \\
\text{Group B} &= \frac{\rho \beta g_x T_s l_s t_s}{\mu} = \frac{\beta g_x k^2 \mu^2}{\rho c_p^2 \frac{\partial \gamma}{\partial T}^3 \Delta T^2} = \frac{Ra}{Ma^3} \\
\text{Group C} &= \frac{\frac{\partial \gamma}{\partial T} t_s T_s}{\mu l_s} = 1 \\
\text{Group D} &= \frac{l_s^2}{\alpha t_s} = \frac{u_s l_s}{\alpha} = 1
\end{aligned}$$

These scalings and associated parameter groupings may be expected to be useful since they are defined simply in terms of the previous classical non-dimensional parameters, and their total number seems to have been effectively decreased by one, since Ra and Ma appear as a ratio. Furthermore, we may expect that for large Ma Group B will be quite reduced in magnitude, and a significant decrease in the importance of the buoyancy term will be realized as a result.

The way in which this choice for l_s effects the geometry of the problem domain is quite important as well. By rewriting Eqn (3.17) we can easily see that:

$$l_s = \frac{k \mu}{\rho c_p \frac{\partial \gamma}{\partial T} \Delta T} = \frac{d}{Ma} \quad (3.18)$$

employing the classical definition for Ma . We thus find that the *a-posteriori* choice for the surface tension length scale is the depth of the problem domain

divided by the Marangoni number. This set of parameters is of course not valid for the case where $Ma = 0$. However, we do see that increasing the Marangoni number effectively shrinks l_s with respect to a fixed domain height d .

If we vary (as is the case with many experimental studies) the aspect ratio of the layer Γ , then for hexahedral domains with height d and horizontal extent Γd , the scaled (computational) domain will have dimensions Ma and ΓMa . Note that increasing Ma is equivalent to increasing the box's dimensions, and it remains to be seen exactly what (if any) effect this will have on computational simulations.

One final disadvantage regarding this formulation is the need to generate a new mesh each time Ma changes. The classical formulation does not suffer from this problem, making it ideal for conducting numerical simulations over a range of Ma using the same mesh each time. However, this does not appear to be a major detraction since we must vary Γ (and therefore change the mesh) throughout the investigation to discover the role that geometry plays in any case.

Chapter 4

Numerical Method

Our objective is to solve the coupled Navier-Stokes, continuity, and heat transfer equations as described in the previous Chapter and rewritten here in full vector form:

$$\rho \left(\frac{\partial \mathbf{u}}{\partial t} + (\mathbf{u} \cdot \nabla) \mathbf{u} \right) = \nabla \cdot \boldsymbol{\sigma} + \rho \beta \mathbf{g} (T - T_{ref}) \quad (4.1)$$

$$\nabla \cdot \mathbf{u} = 0 \quad (4.2)$$

$$\rho c_p \left(\frac{\partial T}{\partial t} + \mathbf{u} \cdot \nabla T \right) = \nabla \cdot (k \nabla T) \quad (4.3)$$

where $\mathbf{u} = (u, v, w)$ is the full velocity vector and $\boldsymbol{\sigma} = -p\mathbf{I} + \mu(\nabla \mathbf{u} + (\nabla \mathbf{u})^T)$. The equations are subject to the boundary conditions given in Table 4.1 and

Table 4.1: Boundary conditions on the governing equations

	Velocity	Temperature
Bottom Surface	$\mathbf{u} = \mathbf{0}$	$T = T_{hot}$
Lateral Walls:	$\mathbf{u} = \mathbf{0}$	$\frac{\partial T}{\partial n} = 0$
Top (Free) Surface	$w = 0$ $\frac{\partial u}{\partial z} = \frac{\partial \gamma}{\partial T} \frac{\partial T}{\partial x}$ $\frac{\partial v}{\partial z} = \frac{\partial \gamma}{\partial T} \frac{\partial T}{\partial y}$	$\frac{\partial T}{\partial z} = \frac{\Delta T}{d}$

are solved in a domain of height d whose upper free surface and no-slip base

are perpendicular to the local gravity vector. The domain is subject to a constant vertical temperature difference given by ΔT . At the free surface, no penetration ($w = 0$) is enforced and traction forces are active in the (non-deforming) plane of the free surface.

We begin by multiplying Eqn (4.1) by a vector test function $\mathbf{v} \in V$, Eqn (4.2) by a scalar test function $q \in Q$, and Eqn (4.3) by $w \in W$, integrating over the domain of interest Ω , and employing the divergence theorem to obtain:

$$\begin{aligned} \int_{\Omega} \left\{ \rho \left(\frac{\partial \mathbf{u}}{\partial t} + (\mathbf{u} \cdot \nabla) \mathbf{u} \right) \cdot \mathbf{v} + \mu (\nabla \mathbf{u} : \nabla \mathbf{v}) - \rho \beta \mathbf{g} (T - T_{ref}) \cdot \mathbf{v} \right\} dV \\ - \int_{\Omega} p (\nabla \cdot \mathbf{v}) dV - \int_{surf.} \frac{\partial \gamma}{\partial T} \nabla T \cdot \mathbf{v} dS = 0 \end{aligned} \quad (4.4)$$

$$\int_{\Omega} (\nabla \cdot \mathbf{u}) q dV = 0 \quad (4.5)$$

$$\begin{aligned} \int_{\Omega} \left\{ \rho c_p \left(\frac{\partial T}{\partial t} + (\mathbf{u} \cdot \nabla) T \right) w + k (\nabla T \cdot \nabla w) \right\} dV \\ - \int_{surf.} (k \nabla T \cdot \mathbf{n}) w dS = 0 \end{aligned} \quad (4.6)$$

where \mathbf{n} is the outward unit normal vector, and we have replaced the surface traction vector $\boldsymbol{\sigma} \cdot \mathbf{n}$ with the temperature-dependent surface tension term: $\boldsymbol{\sigma} \cdot \mathbf{n} = \frac{\partial \gamma}{\partial T} \nabla T$ in Eqn (4.4). Since no-slip boundary conditions have been specified on all parts of the domain except the free surface, we have furthermore required that the respective velocity test functions vanish on the boundary except at the free surface. Finally, with Dirichlet temperature boundary conditions applied to the bottom surface, and the natural (insulating) boundary

conditions applied to the lateral walls, the only remaining boundary term in the energy equation occurs at the free surface.

4.1 Non-dimensionalization

After applying the non-dimensionalization discussed in Section 3.4 one arrives at the following set of equations in place of (4.4)–(4.6):

$$\begin{aligned}
\int_{\Omega^*} \left\{ \frac{1}{Pr} \left(\frac{\partial \mathbf{u}^*}{\partial t^*} + (\mathbf{u}^* \cdot \nabla^*) \mathbf{u}^* \right) \cdot \mathbf{v} + (\nabla^* \mathbf{u}^* : \nabla^* \mathbf{v}) \right\} dV^* \\
- \int_{\Omega^*} \frac{Ra}{Ma^3} \left(T^* - \frac{T_{ref}}{\Delta T} \right) \mathbf{e}_z \cdot \mathbf{v} dV^* \\
- \int_{\Omega^*} p^* (\nabla^* \cdot \mathbf{v}) dV^* \\
- \int_{surf.}^* \nabla^* T^* \cdot \mathbf{v} dS^* = 0
\end{aligned} \tag{4.7}$$

$$\int_{\Omega^*} (\nabla^* \cdot \mathbf{u}^*) q dV^* = 0 \tag{4.8}$$

$$\begin{aligned}
\int_{\Omega^*} \left\{ \left(\frac{\partial T^*}{\partial t^*} + (\mathbf{u}^* \cdot \nabla^*) T^* \right) w + (\nabla^* T^* \cdot \nabla^* w) \right\} dV^* \\
- \int_{surf.}^* (\nabla^* T^* \cdot \mathbf{n}) w dS^* = 0
\end{aligned} \tag{4.9}$$

Note that in these equations, we have already made the assumption that gravity acts only in the z -direction, thus we have been able to replace \mathbf{g} by $g\mathbf{e}_z$ (where g is the magnitude of \mathbf{g}) in Eqn (4.7). This implies that the buoyancy term is only active in the z -momentum equation.

We furthermore note the appearance of the awkward $(T^* - \frac{T_{ref}}{\Delta T})$ term in Eqn (4.7). However, since T^* does not explicitly appear in any other equation except as a gradient, it is quite straight-forward to replace it by some other variable, say $\hat{T} = T^* - \frac{T_{ref}}{\Delta T}$, and taking the gradient, the constant portion vanishes: $\nabla^* \hat{T} = \nabla^* T^*$. Since T_{ref} is the temperature about which the density is expanded in the Boussinesq approximation, it follows that it may be somewhat arbitrarily chosen as $T_{ref} = T_{hot} - \Delta T$ so that the new variable \hat{T} now conveniently varies between 1 at the bottom surface and 0 at the top surface. We shall also, in the remainder of this section, drop the asterisks as a matter of convenience.

The boundary conditions in Table 4.1 in non-dimensional form are given in Table 4.2.

Table 4.2: Non-dimensionalized boundary conditions

	Velocity	Temperature
Bottom Surface	$\mathbf{u} = \mathbf{0}$	$\hat{T} = 1$
Lateral Walls:	$\mathbf{u} = \mathbf{0}$	$\frac{\partial \hat{T}}{\partial n} = 0$
Top (Free) Surface	$w = 0$ $\frac{\partial u}{\partial z} = \frac{\partial \hat{T}}{\partial x}$ $\frac{\partial v}{\partial z} = \frac{\partial \hat{T}}{\partial y}$	$\frac{\partial \hat{T}}{\partial z} = \frac{1}{Ma}$

4.2 Finite Element Method

Proceeding with the finite element method, we now introduce approximation subspaces V_h , Q_h , and W_h for V , Q , and W respectively and define the finite element problem: find $\{\mathbf{u}_h, p_h, \hat{T}_h\}$ satisfying the boundary conditions given in Table 4.1 and such that:

$$\begin{aligned} \int_{\Omega_h} \left\{ \frac{1}{Pr} \left(\frac{\partial \mathbf{u}_h}{\partial t} + (\mathbf{u}_h \cdot \nabla) \mathbf{u}_h \right) \cdot \mathbf{v}_h + (\nabla \mathbf{u}_h : \nabla \mathbf{v}_h) \right\} dV \\ - \int_{\Omega_h} \frac{Ra}{Ma^3} (\hat{T}_h) \mathbf{e}_z \cdot \mathbf{v}_h dV \\ - \int_{\Omega_h} p_h (\nabla \cdot \mathbf{v}_h) dV - \int_{surf.} \nabla \hat{T}_h \cdot \mathbf{v}_h dS = 0 \end{aligned} \quad (4.10)$$

$$\int_{\Omega_h} (\nabla \cdot \mathbf{u}_h) q_h dV = 0 \quad (4.11)$$

$$\begin{aligned} \int_{\Omega_h} \left\{ \left(\frac{\partial \hat{T}_h}{\partial t} + (\mathbf{u}_h \cdot \nabla) \hat{T}_h \right) w_h + (\nabla \hat{T}_h \cdot \nabla w_h) \right\} dV \\ - \int_{surf.} (\nabla \hat{T}_h \cdot \mathbf{n}) w_h dS = 0 \end{aligned} \quad (4.12)$$

hold for *all* admissible \mathbf{v}_h , q_h , w_h . We now introduce the nodal finite element basis functions ϕ_j for the velocity and temperature variables, and ψ_j for the

pressure:

$$u_h^k(\mathbf{x}, t) = \sum_{j=1}^N u_j^k(t) \phi_j(\mathbf{x}) \quad k = 1, 2, 3 \quad (4.13)$$

$$\hat{T}_h(\mathbf{x}, t) = \sum_{j=1}^N \hat{T}_j(t) \phi_j(\mathbf{x}) \quad (4.14)$$

$$p_h(\mathbf{x}, t) = \sum_{j=1}^M p_j(t) \psi_j(\mathbf{x}) \quad (4.15)$$

where each element in the discretized domain Ω_h has $3N$ velocity, N temperature, and M pressure degrees of freedom, $N > M$.

In this investigation we employ the 27-node tri-quadratic velocity and temperature, tri-linear pressure Lagrangian hexahedral finite element (Hex27) in a standard Galerkin formulation. For this element, we have that $N = 27$ and $M = 8$ for N and M given in Eqns (4.13) and (4.15) respectively. Contributions from Eqns (4.10)–(4.12) are computed on each element of the discretized domain, leading to a global system of equations of the form:

$$\mathbf{M}_U \frac{d\mathbf{U}}{dt} + \mathbf{N}_U(\mathbf{U})\mathbf{U} + \mathbf{A}_U\mathbf{U} - \mathbf{F}\mathbf{T} - \mathbf{B}\mathbf{P} - \mathbf{d}_U\mathbf{T} = \mathbf{0} \quad (4.16)$$

$$\mathbf{B}^T\mathbf{U} = \mathbf{0} \quad (4.17)$$

$$\mathbf{M}_T \frac{d\mathbf{T}}{dt} + \mathbf{N}_T(\mathbf{U})\mathbf{T} + \mathbf{A}_T\mathbf{T} - \mathbf{d}_T\mathbf{T} = \mathbf{0} \quad (4.18)$$

where \mathbf{U} , \mathbf{T} , and \mathbf{P} are the unknown velocities, temperatures, and pressures respectively, at the node points. \mathbf{M}_U and \mathbf{M}_E are (symmetric) mass matrices, $\mathbf{N}_U(\mathbf{U})$ and $\mathbf{N}_T(\mathbf{U})$ are nonlinear operators representing the convective terms, \mathbf{A}_U and \mathbf{A}_T are diffusion matrices, \mathbf{F} contains the entries for the buoyant forcing term, \mathbf{B} is the discrete divergence operator, and $\mathbf{d}_U, \mathbf{d}_T$ are the

boundary terms. Matrices denoted with the same symbol, such as \mathbf{M}_U and \mathbf{M}_T come from similar terms in the governing equations, but are not identical due to additional couplings between the components of the velocity vector in the momentum equation.

4.3 Solution Method

A number of methods for decoupling Eqns (4.16)–(4.18) are applicable. For example, the method of Guermond and Quartapelle [12] is used with apparent good success in the work of Medale et. al. [18]. We have attempted such a projection method in our own work, and found it to be quite fast, but it does not produce answers as “correct” as the fully-coupled method. Specifically, the projection method generates well-conditioned matrices, but the resulting flow-fields appear “less incompressible” perhaps due to the Laplacian projection of the pressure.

Time discretization is accomplished with the application of a standard “ θ ” method, i.e. a linear combination of implicit and explicit Euler schemes, in which $\theta = 0$ corresponds to forward Euler, and $\theta = 1$ corresponds to backward Euler. In the time discretization employed in these results, $\theta = 1/2$ (i.e. a Crank-Nicolson scheme) is used.

Eqns (4.16)–(4.18) are linearized using Newton’s method. The method is initialized with a beginning iterate of quiescent flow for the first timestep, and with subsequent starting iterates as the approximate solution at the previous timestep. Once a history of three timesteps has been completed, a

third-order Richardson extrapolation [13] is used to predict an initial guess for the starting iterate in the next timestep. Thus, at each timestep, we must solve a series of sparse, fully-coupled linear systems up to a pre-determined tolerance.

4.4 Computational Aspects

In general, these sparse systems are too large to be tackled with a direct solver, and for fine meshes may in fact be too large to fit on a single workstation. To overcome this difficulty, we have taken advantage of the parallel iterative solvers and preconditioners supplied by the linear algebra software library known as PETSc [1]. Although a large number of iterative algorithms are made available through the PETSc library, an effective preconditioner/solver combination appears to be the Incomplete LU-decomposition (ILU) preconditioner coupled with the transpose-free quasi-minimum residual (TFQMR) iterative solver pioneered by Freund [10].

Besides PETSc, which handles many of the core computations, a few other notable support libraries have been used as well. Static partitioning of the computational domain is handled with the METIS [14] graph-based partitioning library. Inter-processor communication is handled with calls to Message Passing Interface (MPI) [11] routines. Visualization of solutions is accomplished on desktop workstations with the General Mesh Viewer (GMV) [20]. Providing general functionality is a finite element library developed at the University of Texas known as LIBMESH [15].

Chapter 5

Results

5.1 Cellular Patterns With Increasing Aspect Ratio

The first of these numerical results was concerned with the dependence of cellular patterns on aspect ratio. We have chosen a combination of Ra and Ma such that $Ma > Ma_{c,\infty}$ and $Ra \ll Ra_{c,\infty}$ where $Ma_{c,\infty} = 79.6$, $Ra_{c,\infty} = 669$ are the critical Marangoni and Rayleigh numbers predicted by linear analysis. With this choice of values, it is fairly certain that any convective instabilities which occur are almost entirely surface-tension driven.

Figures 5.1 and 5.2 depict a series of steady state solutions on both coarse ($30 \times 30 \times 5$) and fine ($36 \times 36 \times 6$) meshes. (In fact, similar results were obtained for both levels of mesh.) A monotonically increasing number of between 1 and 8 convective cells is observed over a range of aspect ratios between 3 and 11. We stress again that *both* Ma and Ra were held constant during these simulations, implying a strong dependence of the patterns on geometry for these aspect ratios.

Finally, we also note the apparent formation of partial cells near the domain boundaries, especially, for example, in the 2 and 3 cell case. It was decided in these situations to only count cells whose observed centers appeared

somewhere in the interior of the domain. In all cases, the cellular patterns represent an upwelling of the fluid.

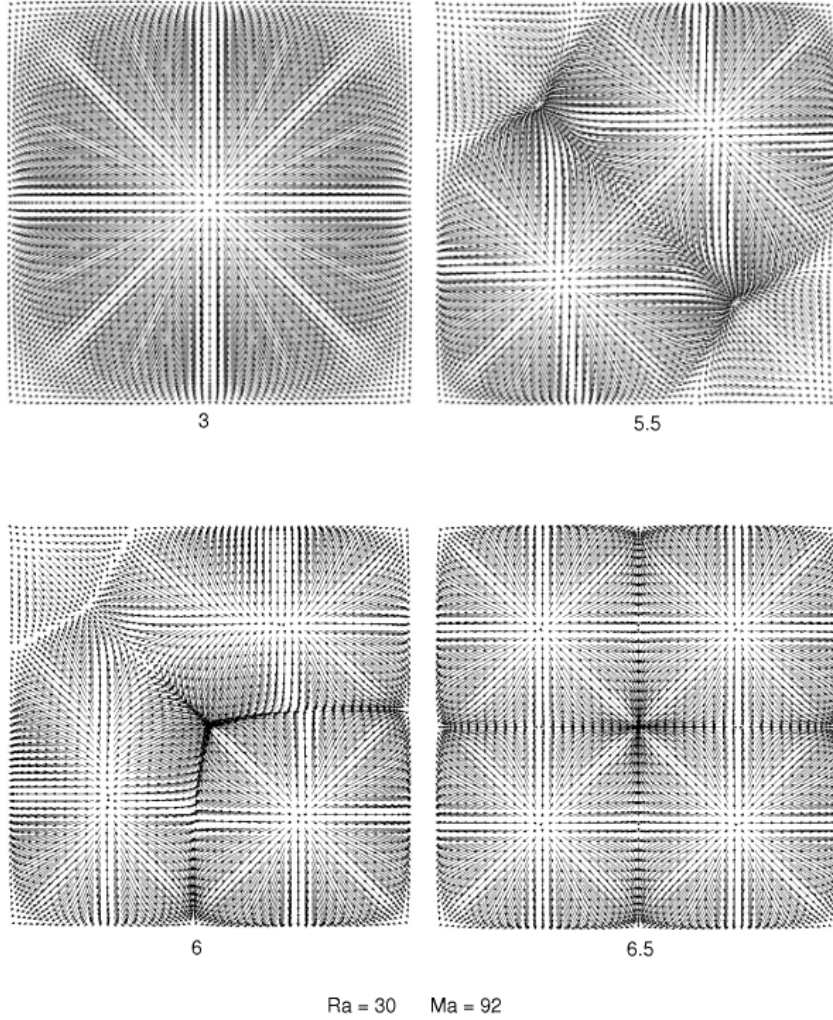


Figure 5.1: Steady states displaying 1, 2, 3, and 4-cell patterns for $Ra = 30$ and $Ma = 92$. The aspect ratios of the domains are given given below each figure. Note that the 2 and 3-cell patterns have additional “partial” cells which are not being counted.

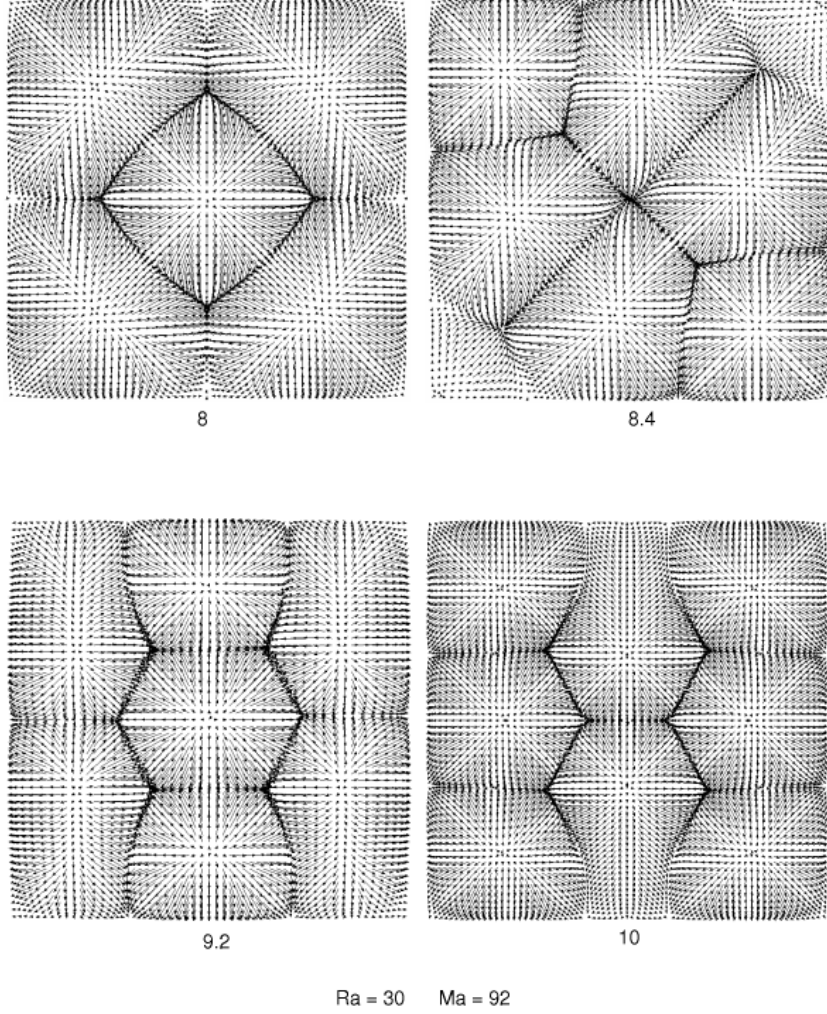


Figure 5.2: Steady states displaying 5, 6, 7, and 8-cell patterns for $Ra = 30$ and $Ma = 92$. The aspect ratios of the domains are given below each figure. The 6-cell pattern has two “partial” cells which are not counted.

5.2 Intermediate Steady States

In this section, we discuss so-called intermediate steady state solutions. They are called intermediate steady states for the simple reason that the cellular patterns which developed appeared to be intermediate to those which have been reported experimentally [17]. This may be due to the fact that a particular set of parameters was never investigated by the experimenters, or that because of uncertainties in experimental parameters, they were simply never seen.

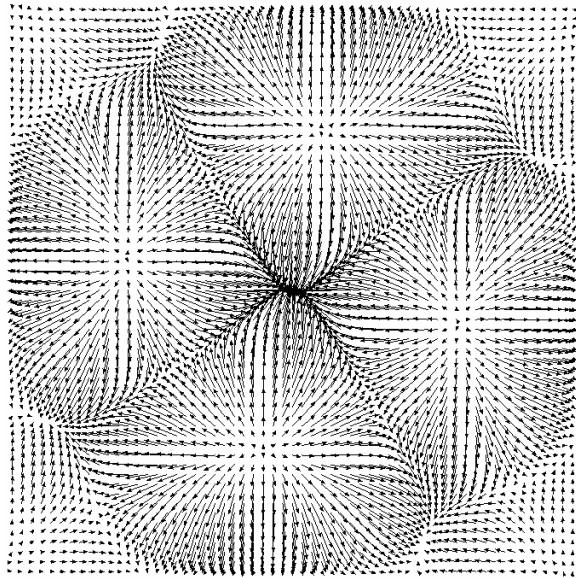


Figure 5.3: Steady state intermediate to the x and y-symmetric 4-cell pattern. At this aspect ratio $\Gamma = 7.5$, it appears that there is not enough space for 5 cells to form, but too much space for the more classic 4-cell pattern to form. Simulation parameters: $Ma = 92$, $Ra = 30$, $\Gamma = 7.5$.

In Figure 5.3, we see an intermediate state between the experimentally

observed 2×2 symmetric 4-cell pattern, and the experimentally observed 5-cell pattern, as shown previously in Figures 5.1 and 5.2. In this case, the steady solution appears to have a clover-like final form. At this aspect ratio, it appears that there is *too much* space for the experimentally-observed 4-cell pattern to occur while there is not yet enough for five cells to form. During the transient phase of the simulation, the solution initially attempts to reach the symmetric 4-cell 2×2 pattern, however two cells along a single diagonal are significantly larger than the remaining two. This appears to force a simultaneous rotation into the steady “clover” configuration shown here.

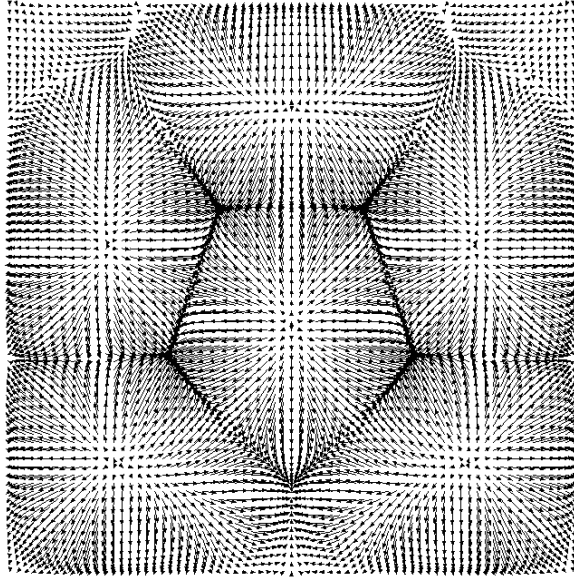


Figure 5.4: The first observed appearance of a pentagonal cell occurred at $\Gamma = 9.0$. In repeated simulations, this state was observed in each of the four possible orientations. Differences in orientation may be attributed to the use of different tolerances and grid resolutions. Simulation parameters: $Ma = 92$, $Ra = 30$, $\Gamma = 9.0$.

In Figure 5.4, we first observe the appearance of a strongly pentagonal cellular structure. This seems a natural central form for a domain containing 6 cells, as 1 cell seems to form along each of the five edges of the central pentagon. The uniaxial symmetry in this case is somewhat difficult to explain, considering that no preferred direction is given to the initial configuration. Similar patterns, defined by 90° rotations of the configuration shown in Figure 5.4 were achievable by adjusting the tolerance of the linear solver and the Newton iteration scheme, as well as using different mesh densities. It appears that in nature, one of the possible patterns would have to be “chosen” due to experimental factors such as thermal noise and imperfections in the container surface.

In Figure 5.5, we note the appearance of a hexagonal structure. The hexagon is the most prevalent shape in large aspect ratio experiments, as evidenced by the experimental work of Bénard himself, and reproduced in Figure 1.2. Although linear theory cannot adequately explain the expected shape of convection cells, nor the fluid’s preference for one cellular structure over another, hexagonal cells are certainly *possible* within the analyses of Chapter 2. Analysis of transitional patterns in small to intermediate aspect ratio containers such as this one may help determine the origin and affinity of such structures. It may be reasoned that the container diagonal, which is a factor of $\sqrt{2}$ longer than the sides of the container, is somehow a more likely location for the hexagonal cell to first appear. This would imply that a hexagonal cell is, in some sense, the “best” or most stable way for convection to pro-

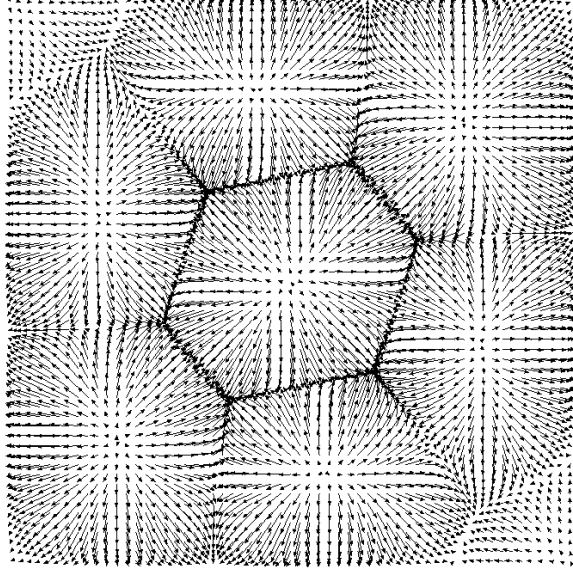


Figure 5.5: The first observed appearance of a hexagonal cell (so common in high aspect ratio experiments) occurred at $\Gamma = 9.25$. It is interesting to note that the hexagonal cell aligns itself with the domain diagonal, where the length dimension is a factor of $\sqrt{2}$ longer than on the domain sides. Simulation parameters: $Ma = 92$, $Ra = 30$, $\Gamma = 9.25$.

ceed in containers above some critical aspect ratio. The results presented here suggest that a possible value for this minimum critical aspect ratio is in the neighborhood of 9.25.

Finally, in Figure 5.6, we present a steady state result from the largest aspect ratio container considered, $\Gamma = 11$. This aspect ratio is larger than any considered in the experiments of Koschmieder. This may be considered a case intermediate to the preceding small aspect ratio examples and the high aspect ratios considered in linear stability analyses. In this example, we may observe 10 convective cells, with an interesting central structure composed of

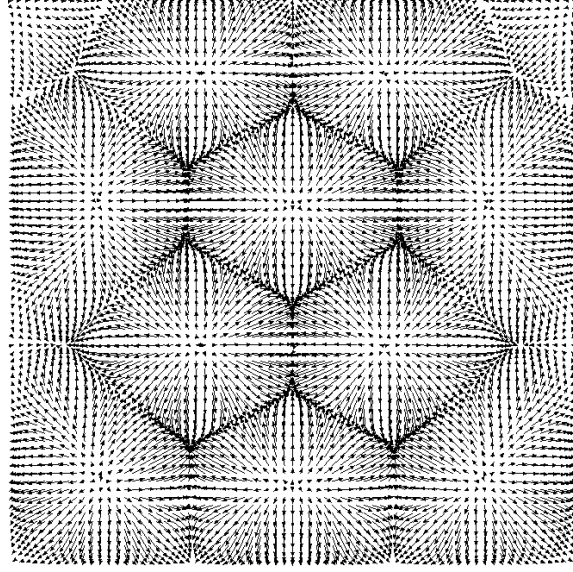


Figure 5.6: The largest aspect ratio attempted in this series of experiments was $\Gamma = 11$. Ten convective cells were observed, with an interesting tessellation of two well-defined pentagonal cells adjacent to a hexagonal cell. With increasing aspect ratio, we expect that the “sharp” vertices of the pentagons will become edges, thereby generating a three-hexagonal structure. Simulation parameters: $Ma = 92$, $Ra = 30$, $\Gamma = 11$.

two pentagonal cells and one hexagon. The cells adjacent to the walls also appear to be relatively pentagonal in nature. With increasing aspect ratio, we may be observing a transition from pentagonal cells to hexagonal cells, with the most regular hexagonal patterns appearing furthest from the walls. This configuration also seems to imply that the “sharpest points” of the pentagonal cells will eventually abut adjacent cells in the manner of the upper hexagonal structures. From this and the preceding results, it seems reasonable to conclude that the pentagon is a versatile transition shape, allowing the cellular

structures to adapt to square domains, and eventually becoming hexagons as the walls of the container influence less and less the central regime of the flow. This conjecture still does not explain why hexagonal cells are preferred in large aspect ratio containers, but does shed some light on the initial formation of such patterns.

Bibliography

- [1] Satish Balay, Kris Buschelman, William D. Gropp, Dinesh Kaushik, Matt Knepley, Lois Curfman McInnes, Barry F. Smith, and Hong Zhang. PETSc users manual. Technical Report ANL-95/11 - Revision 2.1.5, Argonne National Laboratory, 2002.
- [2] H. Bénard. Les tourbillons cellulaires dans une nappe liquide. *Rev. Gén. Sciences Pure Appl.*, 11:1261–1271, 1309–1328, 1900.
- [3] M. J. Block. Surface tension as the cause of Bénard cells and surface deformation in a liquid film. *Nature*, 178:650–651, 1956.
- [4] B. M. Carpenter and G. M. Homsy. Combined buoyant-thermocapillary flow in a cavity. *J. Fluid Mech.*, 207:121–132, 1989.
- [5] C. Cuvelier and J. M. Driessen. Thermocapillary free boundaries in crystal growth. *J. Fluid Mech.*, 169:1–26, 1986.
- [6] S. H. Davis. Buoyancy-surface tension instability by the method of energy. *J. Fluid Mech.*, 39:347–359, 1969.
- [7] H. A. Dijkstra. Structure of cellular patterns in Rayleigh-Bénard-Marangoni flow in two-dimensional containers with rigid side-walls. *J. Fluid Mech.*, 243:73–102, 1992.

- [8] H. A. Dijkstra. Surface tension driven cellular patterns in three-dimensional boxes – I: Linear stability. *Microgravity Science and Technology*, 7(4):307–312, 1995.
- [9] M. F. Schatz et. al. Time-independent square patterns in surface-tension-driven Bénard convection. *Physics of Fluids*, 11(9):2577–2582, 1999.
- [10] R. W. Freund. A transpose-free quasi-minimum residual algorithm for non-Hermitian linear systems. *SIAM J. of Scientific Computing*, 14:470–482, 1993.
- [11] W. Gropp and E. Lusk. User’s guide for MPICH, a portable implementation of MPI. Technical report, Mathematics and Computer Science Division, Argonne National Laboratory, University of Chicago, July 1998.
- [12] J.-L. Guermond and L. Quartapelle. Calculation of incompressible viscous flows by an unconditionally stable projection FEM. *J. Computational Physics*, 132:12–33, 1997.
- [13] M. Heath. *Scientific Computing: An Introductory Survey*. McGraw-Hill Series in Computer Science, 1997.
- [14] G. Karypis and V. Kumar. METIS unstructured graph partitioning and sparse matrix order. Technical report, University of Minnesota, Department of Computer Science, August 1995.
- [15] B. S. Kirk and J. W. Peterson. <http://libmesh.sourceforge.net>. University of Texas at Austin.

- [16] E. L. Koschmieder. *Bénard Cells and Taylor Vortices*. Cambridge University Press, New York, NY, 1993.
- [17] E. L. Koschmieder and S. A. Prahl. Surface-tension-driven Bénard convection in small containers. *J. Fluid Mech.*, 215:571–583, 1990.
- [18] M. Medale and P. Cerisier. Numerical simulation of Bénard-Marangoni convection in small aspect ratio containers. *Numerical Heat Transfer A*, 42:55–72, 2002.
- [19] D. A. Nield. Surface tension and buoyancy effects in cellular convection. *J. Fluid Mech.*, 19:341–352, 1964.
- [20] F. Ortega. <http://www-xdiv.lanl.gov/XCM/gmv/GMVHome.html>. Los Alamos National Laboratory.
- [21] W. B. Patberg, A. Koers, W. D. E. Steenge, and A. A. H. Drinkenburg. Effectiveness of mass transfer in a packed distillation column in relation to surface tension gradients. *Chemical Engineering Science*, 38:917–923, 1983.
- [22] J. R. A. Pearson. On convection cells induced by surface tension. *J. Fluid Mech.*, 4:489–500, 1958.
- [23] L. Rayleigh. On convection currents in a horizontal layer of fluid when the higher temperature is on the under side. *Philosophical Magazine*, 32:529–546, 1916.

- [24] Y. Shen, G. P. Neitzel, D. F. Jankowski, and H. D. Mittelman. Energy stability of thermocapillary convection in a model of the float-zone crystal-growth process. *J. Fluid Mech.*, 217:639–660, 1990.
- [25] F. J. Zuiderweg and A. Harmens. The influence of surface phenomena on the performance of distillation columns. *Chemical Engineering Science*, 9:89–103, 1958.

Vita

During his career as a graduate student, John was a College of Engineering Thrust 2000 fellow as well as a NASA Graduate Student Researcher Program fellow. Research interests beyond Bénard convection include parallel finite element computations, and the development of object-oriented scientific software in C++. He is an active developer for the `libmesh`¹ open source finite element library, and an application code built over this library was used to obtain the numerical results in this report. He hopes to continue on at the University of Texas to obtain a PhD in aerospace engineering.

Permanent address: 2000 Cedar Bend Dr. Apt. 1122
Austin, Texas 78758

This report was typeset with \LaTeX^\dagger by the author.

¹`libmesh.sourceforge.net`

[†] \LaTeX is a document preparation system developed by Leslie Lamport as a special version of Donald Knuth's \TeX Program.